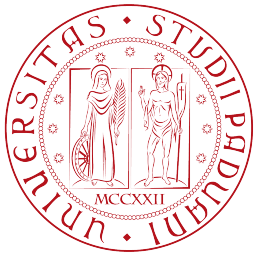

UNIVERSITÀ DEGLI STUDI DI PADOVA

Dipartimento di Fisica e Astronomia "Galileo Galilei"

Corso di Laurea in Fisica

Tesi di Laurea

Preliminary plasma parameter estimation by means of emission spectroscopy in a new ICP discharge experiment at the ITER Neutral Beam Test Facility

Stima preliminare dei parametri di plasma tramite spettroscopia di emissione in un nuovo esperimento a scarica induttiva presso la Neutral Beam Test Facility di ITER

Relatore

Dott. Gianluigi Serianni

Correlatore

Dott. Isabella Mario

Laureanda

Martina Tesser

Anno Accademico 2023/2024

ABSTRACT

Neutral Beam Injectors for fusion applications require the production and acceleration of negative ions. Negative ion sources are based on the inductive coupling of electromagnetic waves to a hydrogen plasma (ICP discharge). To optimise the design of such sources, and particularly of the RF driver (the region where the plasma is generated), the MINION experiment was designed and realised at Consorzio RFX. Within the first MINION experimental campaign, measurements of hydrogen plasma emission by a spectroscopic system have been performed, with the aim to characterize the plasma parameters in the region of the ion source where the ICP plasma is ignited. The plasma parameters will be evaluated with the assistance of collisional radiative models. Plasma parameter evaluation will be repeated under different operational conditions (e.g. RF power, pressure).

ABSTRACT

Gli iniettori di neutri per la fusione nucleare richiedono la produzione e accelerazione di ioni negativi. Le sorgenti di ioni negativi sono basate sull'accoppiamento induttivo delle onde elettromagnetiche con un plasma di idrogeno (Inductive Coupling Plasma discharge). Per ottimizzare la struttura di queste sorgenti e in particolare del driver RF, ossia la regione in cui viene generato il plasma, è stato realizzato al Consorzio RFX l'esperimento MINION. Nella prima campagna sperimentale con MINION sono state raccolte misure del plasma di idrogeno attraverso la spettroscopia di emissione, con l'obiettivo di caratterizzare i parametri di plasma nella regione della sorgente di ioni, dove viene acceso il plasma ICP. I parametri di plasma saranno valutati sfruttando modelli radiativo-collisionali e le misure saranno effettuate sotto diverse condizioni operative, variando la potenza RF e la pressione.

Contents

Chapter 1

Introduction

1.1 Fusion

ITER (the *path* towards fusion energy), the first experimental nuclear reactor, based on a worldwide collaboration, aims at demonstrating the scientific and technological feasibility of fusion as a large-scale source of energy [7] [8]. Fusion power plants based on magnetic confinement are expected to provide a reliable, safe and environmentally low-impact source of energy [9]. ITER aims to achieve a gain of 10, defined as the ratio between the output fusion power and the input heating power. To increase the probability of the fusion process to happen, the particle energy needs to be sufficiently high to overcome the Coulomb barrier between the nuclei; therefore, ITER is meant to work with hot plasmas, which have temperatures in the order of 10^8 K.

To achieve this requirements, ITER will feature two[1] heating Neutral Beam Injectors (NBI) based on radio frequency (RF) driven plasmas which will provide the fusion plasma with a total power of $33.3MW$ with either a $1MeV$ deuterium beam or $0.87MeV$ hydrogen beam, for up to 3600 s. Each NBI consists of a $2m$-high, $1m$-wide Inductively-Coupled Plasma (ICP) for production of hydrogen or deuterium negative ions [6]. The negative ions are extracted and accelerated in a multi-aperture multi-grid (MAMuG) [1] electrostatic accelerator with a 7 grid system up to a maximum energy of $1MeV$. Before the injection into the fusion chamber, where their energy is deposited into the fusion plasma via collision, or onto a calorimeter [13], the beam is neutralized, and the residual ions are electrostatically removed. The choice of neutralizing negative ions instead of positive ions is based on the neutralization efficiency, due to the low binding energy of the second electron for negative ions: the neutralization efficiency at $1\,MeV$ for positive ions is a few %, whereas for negative ions it is 60% and quite independent of the energy. However, this choice leads to two more stringent requirements for ITER, namely the requirement on the pressure is ≤ 0.3 Pa in the ion source and the grid system, to minimize the loss of negative ions via collision with the background gas (stripping), and the ratio between co-extracted electrons and the extracted negative ions has to be lower than 1, to minimize the power load on the surfaces where co-extracted electrons are dumped. Moreover, ITER requires the extracted current density in hydrogen to be 329 A/m^2 for the heating neutral beam (HNB) and 355 A/m^2 for the diagnostic neutral beam (DNB), whereas in deuterium it has to be 285 A/m^2 for the HNB. Also, the beam is composed of 1280 beamlets and the beam inhomogeneity has to be such that the current of each beamlet differs from the average by less than $\pm$10%. The ITER NBI requirements aim at ensuring beam transmission through the 26 m long beamline up to the fusion plasma.

SPIDER (Source for the Production of Ion of Deuterium Extracted from Rf plasma) is the full-size RF-driven, negative-ion source for ITER NBIs. SPIDER has operated from 2018 to 2021 at the Neutral Beam Test Facility (NBTF) in Consorzio RFX, Padova, and the operations were devoted to characterizing the source plasma, the beam and the 4 RF oscillators, each one feeding two drivers connected in series. In order to make changes to the experimental setup, SPIDER has not been

[1] A third NBI may be installed at a later stage.

operating since 2021, but a new campaign is planned to start by April 2024.

Moreover, most of the plasma grid apertures were masked by a thin molybdenum layer to limit the required gas flow. This permitted to perform detailed measurements of the beamlet divergence, which was shown to exceed the target value for ITER (12 $mrad$ instead of the $3.5 - 7$ $mrad$ range required by ITER). Since numerical models predict a much lower divergence for a colder negative ion beam, a new experiment, MINION, has started, with the aim of modifying the plasma parameters into more convenient values. Hence, the proposal to install permanent magnets in the electrostatic shield outside the RF driver, to increase the plasma density and diminish the plasma potential, thus reducing the beamlet divergence.

1.2 The MINION Experiment

The MINION (Magnetized ICP for Negative Ion Operation in NBI) experiment consists of an ion source with a single RF driver, identical to the SPIDER RF drivers, connected to a plasma box. The ion source is installed inside a vacuum vessel having a cylindrical lateral wall with hemispherical domes at the top and bottom. The vessel is divided in two halves: the upper part is supported by a metallic structure, whereas the lower part of the vessel lies on a movable motorized support, which allows for vertical movements and horizontal movements on tracks on the floor level.

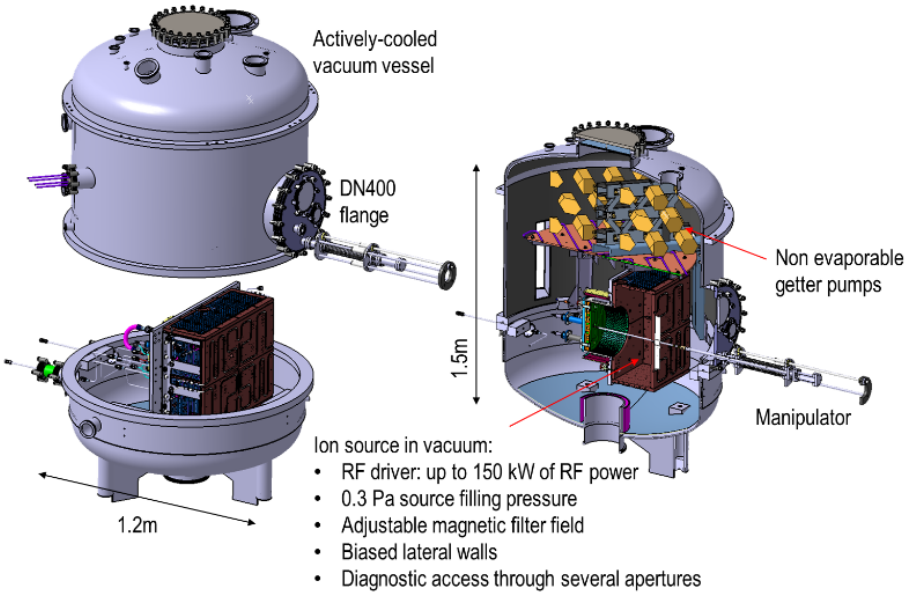

Figure 1.1: Schematic of the MINION experiment, with the vacuum vessel in grey and the plasma source in brown. On the left, the large DN400 diagnostic flange where a manipulator is mounted. On the right, a vertical section, when the vessel is closed, is shown. In the drawing, the manipulator is fully inserted in the ion source, the non-evaporable getter pump system is shown on the top.

In figure 1.1, the setup of the vacuum vessel closed (right) and open (left) is shown. On the lower vessel part, the plasma source (RF driver and plasma box) is placed, optimal for maintenance of the in-vacuum components. The plasma box is 22 cm-deep, 57 cm-large and the height is 50 cm. The vacuum vessel features a large DN 400 flange and the plasma source is positioned and oriented in the vacuum vessel to face the DN 400 flange, which holds a horizontal manipulator. The manipulator (see Figure 1.2) supports a Langmuir probe (LP) that moves along the driver axis and can reach the back side of the RF driver, the so-called driver backplate.

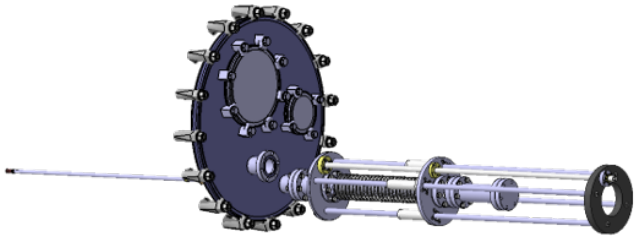

Figure 1.2: Schematic of the manipulator used to support and move the Langmuir probe in the ion source.

The magnetic field in MINION is produced by permanent magnets arranged on either side of the plasma box. The vacuum system consists of two turbomolecular pumps[2], two cryogenic pumps[3] and a forevacuum screw pump[4]. A mass flow controller (MFC) injects hydrogen gas into the plasma source through the back of the driver. The cooling systems supply the RF driver components, whereas the plasma box is inertially cooled in the present realization.

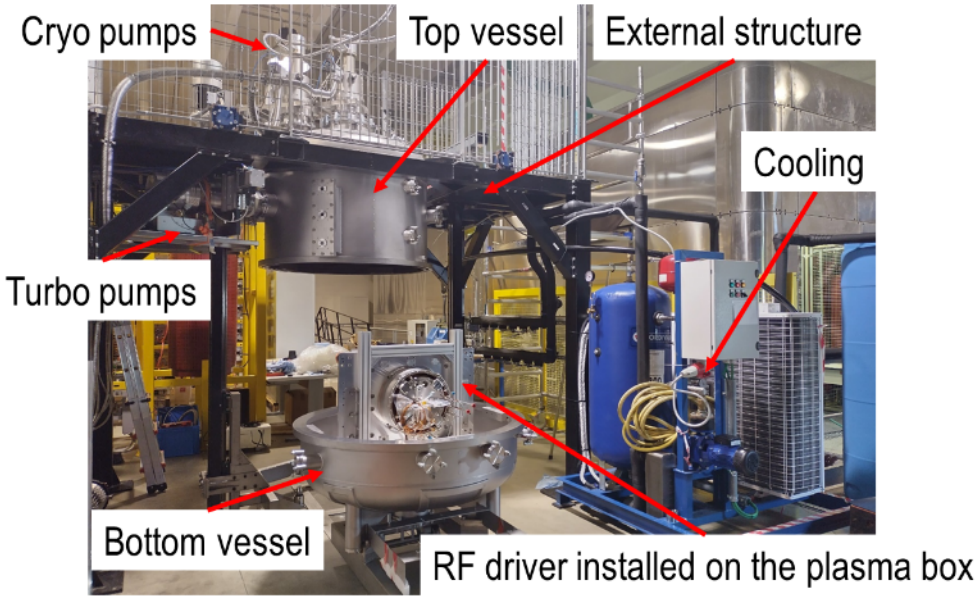

Figure 1.3: Picture of the MINION experiment with the vacuum vessel open, and plasma box mounted on the bottom vessel part. Some features of the vacuum and cooling systems are highlighted.

1.3 Plasma and atomic physics overview

A plasma is a (partially or fully) ionized gas with the property of quasi-neutrality, which means that the electron density is similar to the positive ion density, and is characterized by a collective behaviour. The quasi-neutrality hypotheses originates from considering a system where a net charge q is put inside a single ionized plasma characterized by n_e and n_i, the electron and ion density, respectively. The electrostatic potential ϕ follows the Poisson equation:

$$\nabla^2\phi = -\frac{e}{\varepsilon_0}(n_i - n_e) - \frac{q\delta(r)}{\varepsilon_0} \tag{1.1}$$

[2]MAGINTEGRA 1300
[3]COOLVAC 1.500 CL
[4]ScrollVac 18 plus

Denoting with T the temperature (equal for electrons and ions) and with n the density far from the charge, then

$$\begin{aligned} n_e &= n\ exp\Big(\frac{e\phi}{k_B T}\Big) \\ n_i &= n\ exp\Big(-\frac{e\phi}{k_B T}\Big) \end{aligned} \tag{1.2}$$

where $k_B = 1.38 \cdot 10^{-23}\, K^{-1}$ is the Boltzmann constant; if the argument of the exponential function is much less than 1, then the Poisson equation can be rewritten via Taylor expansion until first order as

$$\nabla^2 \phi \approx \frac{2\phi}{\lambda_D^2} - \frac{q\delta(r)}{\varepsilon_0} \tag{1.3}$$

where

$$\lambda_D \equiv \sqrt{\frac{\varepsilon_0 k_B T}{n e^2}} \tag{1.4}$$

is the Debye length. Equation 1.3 can be easily solved

$$\phi(r) = \frac{q}{4\pi\varepsilon_0 r} exp\Big(-\frac{\sqrt{2}r}{\lambda_D}\Big) \tag{1.5}$$

The solution implies that λ_D is the length required to screen a free charge immersed in the plasma and that outside of that region the effect of the charge is negligible; therefore, plasma quasi-neutrality, even though it can be violated in small regions, is globally valid in the plasma.

Moreover, because of the difference between the electron and ion masses, the electron mobility is higher and therefore their reaction to electric fields is quicker. As the electrons move, they create another electric field, the ambipolar electric field, which pulls the positive ions maintaining the quasi-neutrality. The plasma frequency f_{pe} defines a time scale for the restoration of quasi-neutrality, while the Debye length defines the spatial scale of the region where quasi-neutrality can be violated.

$$f_{pe} = \sqrt{\frac{e^2 n_e}{\varepsilon_0 m_e}} \tag{1.6}$$

with m_e the electron mass, n_e the electron density, ε_0 the vacuum electrical permittivity.

Related to the Debye length, the *plasma parameter* $\Lambda = 4\pi\lambda_D^3 n_e$ is used to divide strongly coupled plasma ($\Lambda \ll 1$) and weakly coupled plasma ($\Lambda \gg 1$).

In Niels Bohr's atomic model, electrons are revolving around the nucleus, following circular, stationary orbits, at fixed energies; also, electrons can move from one allowed orbit to another, with the consequent gain or loss of energy. The frequency of the emitted -or absorbed- electromagnetic wave is given by the Planck relation

$$|E_f - E_i| = h\nu \tag{1.7}$$

where E_f and E_i are the energies of the final and the initial orbit respectively, ν is the wave frequency and $h = 6.626 \cdot 10^{-34} J/s$ is the Planck constant.

By considering the simplicity of the hydrogen atom, it is possible to derive the equation of motion for the electron:

$$\begin{cases} \frac{\mu v_n^2}{r_n} = \frac{e^2}{4\pi\varepsilon_0 r_n^2} \\ \mu v_n r_n = n\hbar \end{cases} \tag{1.8}$$

where v_n and r_n are the velocity and the radius of the electron in the orbit n; μ is the reduced mass, e the elementary charge, $\hbar$ the reduced Planck constant, $\hbar = h/(2\pi)$.

From these equations, the energy in the orbit n is given by

$$E_n = \frac{1}{2}\mu v_n^2 - \frac{e^2}{4\pi\varepsilon_0 r_n} = -\frac{me^4}{32\pi^2\varepsilon_0^2\hbar^2 n^2} \tag{1.9}$$

By taking in mind Bohr's hypotheses and by analysing the transition of a bound electron between an orbit with $n = p$ and an orbit with $n = q$, where $p > q$, it is possible to derive the Rydberg's equation for the energy of the photon emitted during the electron transition:

$$h\nu = E_p - E_q = R_H \left(\frac{1}{p^2} - \frac{1}{q^2}\right) hc \tag{1.10}$$

where $R_H = \frac{me^4}{8\varepsilon_0^2 h^3 c} = 1.09677583 \cdot 10^7\, m^{-1}$ is the Rydberg constant and c is the speed of light in vacuum.

1.4 Spectroscopy

Spectroscopy is a branch of Physics that has the aim of studying the interaction between light and matter. In the simplified case of the hydrogen atom, the interaction between the electron and light can lead to three different phenomena: stimulated emission, absorption, spontaneous emission. All of them involve the electron transition between energetic levels, whose energies are described by Rydberg's formula despite being three completely different physical situations: stimulated emissions happen when an incoming photon interacts with an upper-state electron, causing it to fall into a lower state, with the emission of a photon carrying the energy, polarization and direction of the incoming photon. Absorption happens when an electron in a lower energy level interacts with a photon carrying an energy comparable to the energy difference of two electronic levels and gains its energy, transitioning to the higher level. Spontaneous emission is the process where, from an upper state, the electron falls into a lower state and emits a photon with the same energy as the energy difference between the upper and the lower level. Only the transitions that follow the selection rules are allowed, namely only between states with $\Delta l = \pm 1$ and $\Delta m = 0, \pm 1$ (with Δl the difference of angular quantum number and Δm the difference of magnetic quantum number).
The intensity of emission that follows a transition between two energy levels is directly correlated to the density population, which, in turn, depends strongly on the plasma parameters, as it follows

$$\varepsilon_{pq} = n(p)\, A_{pq}\, \frac{hc}{4\pi\lambda_0} \qquad [Wm^{-2}sr^{-1}] \tag{1.11}$$

where $n(p)$ is the excited state density, the energy level is indicated with the quantum number $n = p$ and A_{pq} is the Einstein coefficient. The central wavelength of the line emission in analysis is indicated with λ_0 and is defined as:

$$\lambda_0 = \frac{hc}{E_q - E_p} \tag{1.12}$$

Therefore, the density in the excited state p depends on the processes occurring in the plasma. In chapter 1.6 the relation is more specifically explained.

Optical Emission Spectroscopy (OES) focuses on spontaneous emissions and is used as plasma diagnostics, since coupled with codes predicting excited state density, it allows for the estimation of plasma parameters, such as electron temperature and electron density. OES is commonly used in fusion plasmas because, unlike Langmuir probes, it does not cause any disturbance to the plasma itself. On the other hand, OES does not yield localized measurements, since the emission is collected along a line of sight (LOS). In order to obtain quantitative results with OES, the spectroscopic system needs to be calibrated in advance, so that from the measured spectra the number of emitted photons can be deduced, giving direct access to the estimation of plasma parameters [3] (see Section 1.7).

The relation between emission lines and wavelengths allows interpreting spectra, which are arrangements of the intensities of the emission lines according to the wavelength they are referring to. For

hydrogen atoms, the emission lines are labelled with different names by taking into account the final orbit for the electron transition, as shown in Figure 1.4. In the MINION driver, the transitions in the visible range are the ones with final orbit $n = 2$, constituting the so-called Balmer series, reported in Table 1.1.

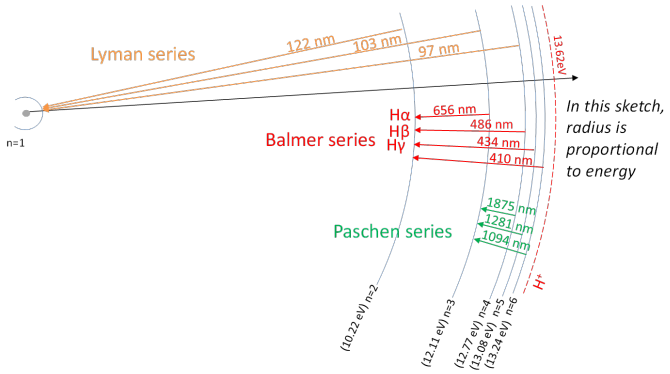

Figure 1.4: Excited levels of hydrogen atom; the Lymann series is in the UV range, while the Paschen series is closer to the IR range.

line name	initial orbit	$\lambda[nm]$
H_α	3	656.3
H_β	4	486.1
H_γ	5	434.0
...	...	...

Table 1.1: Balmer series and respective corresponding wavelengths

Other than the species that characterize the plasma (H atoms and H_2 molecules), OES is useful to identify also the impurities that affect the experiment, such as O_2 and Cu. Having the possibility to keep under control the increase in the oxygen emissions or copper emissions is critical to identify malfunctioning without opening the experiment and most importantly before irreparable damage ensues.

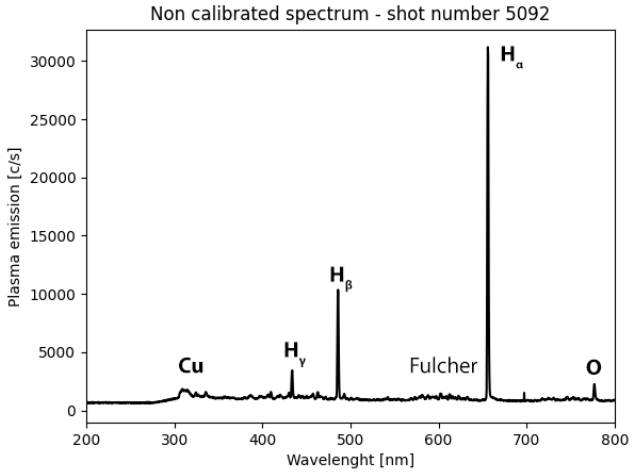

Figure 1.5: Example of spectrum, acquired during an RF pulse: the main emissions are labelled. The spectrum is shown before applying the calibration procedure.

The probability (per unit time, volume and solid angle) that a spontaneous emission takes place is given by the Einstein coefficients

$$A_{pq} = \frac{(E_p - E_q)^3}{3\pi\varepsilon_0\hbar^4 c^3}\left|\langle q|\,\vec{d}\,|p\rangle\right|^2 \tag{1.13}$$

where $\vec{d} = -e\vec{r}$ is the electric dipole operator and the Dirac notation is used to denote the transition between the initial state p and the final state q.

The first three Einstein coefficients for the Balmer series are listed in Table 1.2.

line name	coefficient	values $[s^{-1}]$
H_α	A_{32}	$4.41078 \cdot 10^7$
H_β	A_{42}	$8.42076 \cdot 10^6$
H_γ	A_{42}	$2.53115 \cdot 10^6$

Table 1.2: Einstein coefficient for H_α, H_β, H_γ

De-excitations, collision processes, and spontaneous emission from the excited states are the main ones in terms of populating and de-populating the atom states. Whereas the probability for spontaneous emission is described by Einstein coefficients (1.13), collisions are characterized by rate coefficients or, for each energy, by cross sections. If the electron energy distribution is described by a Maxwellian distribution, $f(E)$, the rate coefficients can be defined as a function of both the Maxwellian distribution and the cross section $\sigma(E)$

$$X^{exc}(T_e) = \int_{E_{thr}}^{\infty} \sqrt{\frac{2}{m_e}}\sigma(E)\sqrt{E}f(E)dE \tag{1.14}$$

with

$$\int_0^{\infty} f(E)dE = 1 \tag{1.15}$$

and E_{thr} the threshold of the electrons' energy that actually contributes to the excitation rate coefficient. The Maxwellian distribution $f(E)$ is defined as follows:

$$f(E) = \sqrt{\left(\frac{m}{2\pi k_B T}\right)^3} 4\pi v^2 e^{-\frac{mv^2}{2k_B T}} \tag{1.16}$$

Figure 1.6 shows the cross sections concerning the collisions between the hydrogen atom and one electron, that excite the atom up to the upper levels; it highlights the existence of a well-defined value of energy threshold. Specifically the processes are

$$\begin{aligned} e, H[1s] &\longrightarrow e, H[n=3] \\ e, H[1s] &\longrightarrow e, H[n=4] \\ e, H[1s] &\longrightarrow e, H[n=5] \end{aligned} \tag{1.17}$$

The de-excitation from these three excited levels down to the $n = 2$ state results in the first, the second and the third Balmer line, as explained in the previous section.

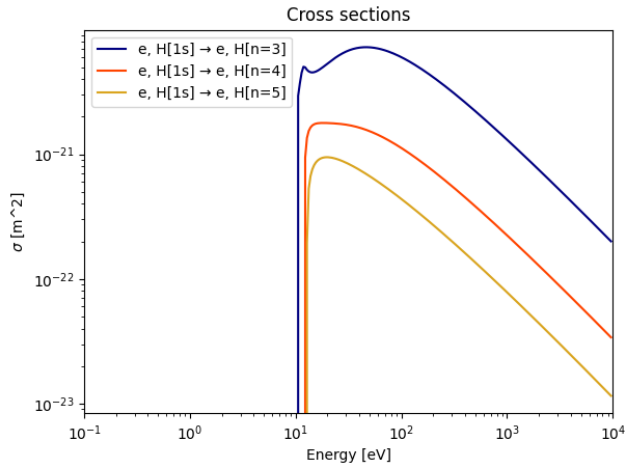

Figure 1.6: Cross sections as a function of the electron energy

1.5 Models to interpret OES measurements

To simplify the interpretation of spectral lines intensity and develop methods for the determination of plasma parameters, it is important to specifically characterize the different types of plasma. The condition under which a plasma is to be considered in local thermodynamic equilibrium (LTE) is that the population density of the quantum level p must be described by the Saha-Boltzmann equation [4]

$$n_{SB}(p) = [n(gs)]^{+} n_e \frac{g(p)}{2[g(gs)]^{+}} \Big(\frac{h^2}{2\pi m k_B T_e}\Big)^{\frac{3}{2}} exp\Big(\frac{\chi(p)}{k_B T_e}\Big) \tag{1.18}$$

where n_{SB} and $g(p)$ are the Saha-Boltzmann population density and statistical weight, respectively, of level p, the symbol "+" refers to the ion having charge greater than the level p by 1 and gs stands for ground state. χ is the ionization potential, k_B the Boltzmann constant, h the Planck constant, n_e and T_e the electron density and temperature respectively.

Equation 1.18 shows that only a plasma with electron density higher than $n_e \sim 10^{22} m^{-3}$ can satisfy LTE conditions.

On the other hand, in plasmas with a very low electron density ($\sim 10^{16} m^{-3}$) the population density does not follow the Saha-Boltzmann equation (Equation 1.18), but is described by the corona model, which assumes that, for downwards transitions, the vast majority of the de-excitation processes due to electron collisions are negligible, so the discussion is reduced to the study of spontaneous emissions that happen as a consequence of the excitation of the hydrogen atom by electron collision

$$H(q) + e^{-} \longrightarrow H(p > q) + e^{-} \tag{1.19}$$

At the same time, in corona models, upwards transitions are to be attributed to electron collisions. Therefore the population of an excited state p is balanced by electron impact excitation from the ground state $q = 1$ and decay by spontaneous emission

$$n_1 n_e X_{1p}^{exc}(T_e) = n_p \sum_k A_{pq} \tag{1.20}$$

where $X_{1p}^{exc}(T_e)$ is the previously discussed rate coefficient and A_{pq} is Einstein coefficient. Due to the fact that populations of excited levels are orders of magnitude lower than the population of the ground state, $n_1 \sim n_n$ with n_n the overall particle density [3].

Either way, the particle density in the driver region is about $10^{17} - 10^{18}\, m^{-3}$ (see Section 2.3), therefore the most suitable model is the Collisional Radiative (CR) model. The approach is to define rate equations for each particle state, so as to take into account every process taking place in the plasma.

The time evolution of population densities is described by a sum of many terms, each one describing a different process contributing to the time evolution

$$\begin{aligned}\frac{\mathrm{d}n(p)}{\mathrm{d}t} = &\underbrace{\sum_{q<p} n(q) n_e X_{qp}^{\mathrm{exc}}}_{excitation} - \underbrace{n(p)\left[n_e\left(\sum_{q<p} X_{pq}^{\mathrm{de-exc}} + \sum_{q>p} X_{pq}^{\mathrm{exc}} + S_p\right) + \sum_{q<p} A_{pq}\right]}_{de-excitation} \\ &\underbrace{+n(q)\sum_{q>p}\left(n_e X_{qp}^{\mathrm{de-exc}} + A_{qp}\right)}_{three\ body\ recombination} + \underbrace{n_i n_e\left(n_e\alpha_p + \beta_p\right)}_{radiative\ recombination}\end{aligned} \tag{1.21}$$

In the driver region, the two main processes are the previously discussed excitation by electron collision (see 1.19), which contributes to emission for $\sim 70\%$, and the dissociation of H_2, even though the latter happens with far lower probability ($\sim 20\%$)[9].

$$H_2 + e^- \longrightarrow H(p) + H(gs) + e^- \tag{1.22}$$

with gs indicating the ground state.

The remaining $\sim 10\%$ is to be attributed to dissociative recombination.

$$H_2^+ + e^- \longrightarrow H(p) + H(gs) \tag{1.23}$$

Hence, in the driver region the plasma is ionizing. Under this condition, the terms of Equation 1.21 which do not relate to the mentioned processes can be neglected and in quasi-steady conditions the time derivative is zero, so that the equation has a simple solution:

$$n(p) = R_n(p) n_n n_e + R_i(p) n_i n_e \tag{1.24}$$

with $R_n(p)$ and $R_i(p)$ the rate coefficient describing population processes from the ground state and from the ion state, respectively.

In the following analysis, the only process taken into account is the direct excitations.

1.6 Line ratio method

In section 1.4 it has been highlighted that the emission intensities are strongly correlated to the population density, by equation 1.11. Conveniently, one can describe the intensity of emission by using the absolute line intensity I_{pq}, so that the unit of measurement can be directly linked to the number of photons

$$I_{pq} = n(p) A_{pq} \qquad [photons\ m^{-2} s^{-1}] \tag{1.25}$$

Based on the CR model and assuming the conditions in which it can be applied are satisfied, the line ratio method can be used to determine the plasma parameters. The line method is based on the comparison between the measured emission lines and the emission lines, calculated through combination of equations 1.24 and 1.25

$$\frac{I_{pq}}{n_e n_n} = \frac{n(p) A_{pq}}{n_e n_n} = \frac{R_n(p) n_n n_e + R_i(p) n_i n_e}{n_e n_n} A_{pq} = (R_n(p) + R_i(p)\frac{n_i}{n_n}) A_{pq} = X_{pq}^{eff} \tag{1.26}$$

While in the corona model the population in excited states depends on the electron temperature only, in the CR model it depends also on temperature and density populations of other species (e.g. the neutrals), so that X_{pq}^{eff}, the rate coefficient, is also a function of both electron temperature and density.

Defining two more principal quantum numbers, m and n, other than p and q, the emission line ratio becomes:

$$\frac{I_{pq}}{I_{mn}} = \frac{n_e n_n X_{pq}^{eff}}{n_e n_n X_{mn}^{eff}} = \frac{X_{pq}^{eff}}{X_{mn}^{eff}} \tag{1.27}$$

and in the specific case of the plasma under analysis, the interesting line ratio is:

$$\frac{I_{32}}{I_{42}} = \frac{I_{H_\alpha}}{I_{H_\beta}} = \frac{X_\alpha^{eff}}{X_\beta^{eff}} \tag{1.28}$$

The line ratio method is therefore a powerful tool to interpret spectra because it allows a comparison between the rate coefficient ratios, which are computed on accurate basis and therefore are valid values to rely on, and the experimental emission lines ratios, which are described in section 2.3.

1.7 Calibration procedure

An optical system needs to be calibrated both in terms of wavelength and intensity. The wavelength calibration is needed to univocally associate a pixel position on the CCD camera to a wavelength. To do so, mercury lamps are used, because of the low electron temperature and consequent small Doppler broadening of the emission lines; emission lines are particularly narrow, in fact, and by comparing them with the tabulated ones [14], it is possible to calibrate the wavelength axis.

The most complex calibration is the one regarding the intensity axis, the so-called absolute calibration. The absolute calibration is needed to convert the CCD camera counts into a value of $photons\ m^{-2}s^{-1}$. To do so, an intensity-calibrated light source, for which the spectral radiance is known, is required. To this purpose, an Ulbricht sphere, or integrating sphere, [2] was used. Its functioning is based on the notion that light incident on a diffuse surface creates a virtual light source by reflection, which is best described by its radiance. Radiance, L, is defined as the flux density per unit solid angle and unit projected area ($Wsr^{-1}m^{-2}$). Calibration curves are given in terms of $Wsr^{-1}m^{-2}nm^{-1}$, and the spectral width of the pixel must be multiplied to the calibration curve, to obtain the flux density in terms of $Wsr^{-1}m^{-2}$. The calibration follows three steps: the first is the conversion from radiance to number of photons per unit solid angle per unit area, done by using the notion that one photon carries an energy of $h\frac{c}{\lambda}$ to obtain

$$\frac{photons}{m^2 s} = L\frac{\lambda}{hc} \tag{1.29}$$

Then, the calibration procedure requires the analysis of the spectrum collected with the spectrometer pointing at the Ulbricht sphere, through the optical chain, which consists of the optical items (filters, fibers, telescopes, feedthrough) connecting the spectrometer to the light source that needs to be studied.

Finally, the calibration curve is applied to the non-calibrated spectra to obtain calibrated spectra, to be used for further analyses.

Chapter 2

Experimental activity

For the calibration procedure, two different setups were used. This is due to the fact that in the first setup the plasma light was too bright to fit inside the range of intensities of the spectra, despite decreasing the exposure time down to its minimum (10 ms)[1]. Therefore, in the second setup, two Neutral Density 1.0 ($ND1$) filters, each one filtering about 90% of the emission light, were added in order to dim the plasma light. The type of filter was chosen because they reduce the intensity at all wavelengths. The wavelength calibration remains the same after adding the filters, but the intensity calibration changes. Setup 0 was used for the first 67 sets of data, setup 1 for the rest of the data, as specified in Table 2.1.

	range of shots
setup 0	5026-5093
setup 1	5094-5342

Table 2.1: Distribution of the different shots depending on the setup used for the calibration phase.

The spectra analysed in this work are obtained in MINION through the line-of-sight shown in Figure 2.1, identified as $LOS1$. The spectrometer that was linked to the $LOS1$ is a model $TM series$, $C10082CAH$[2]

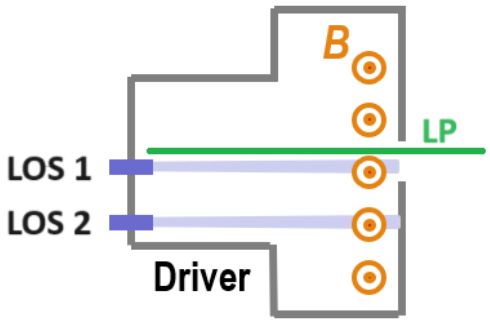

Figure 2.1: Schematic representation of the LP probe position inside the drive and of two of the line of sights available in MINION; LOS 1 is the one used for the following analysis.

[1]The exposure time has a minimum because the shutter, which is the mechanical system that opens and closes the diaphragm, for exposure times lower than the minimum cannot open and close fast enough.

[2]Mini-spectrometers C10082CA/C10083CA series (`hamamatsu.com`)

2.1 Optical system calibration

2.1.1 Wavelength calibration

To properly calibrate the wavelength axis, is needed to assess the angle of the diffraction grating, which is placed before the CCD device on the path of light. This allows to obtain the relation between wavelengths and the CCD pixels (Figure 2.2).

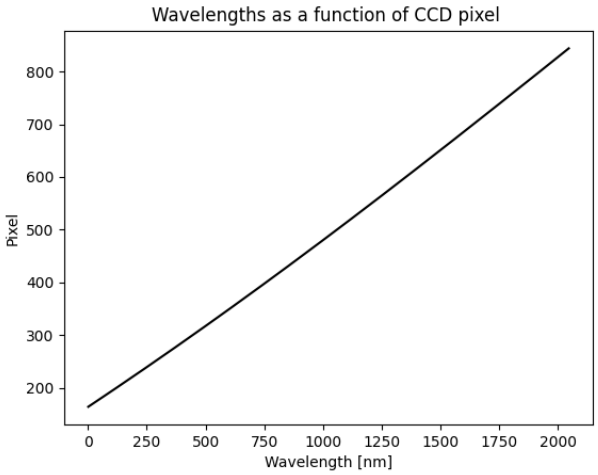

Figure 2.2: Relation between CCD pixels and wavelength.

Figure 2.3 shows the spectrum (shot number 5226) as a function of the CCD pixels (left) and the same spectrum as a function of the wavelengths (right).

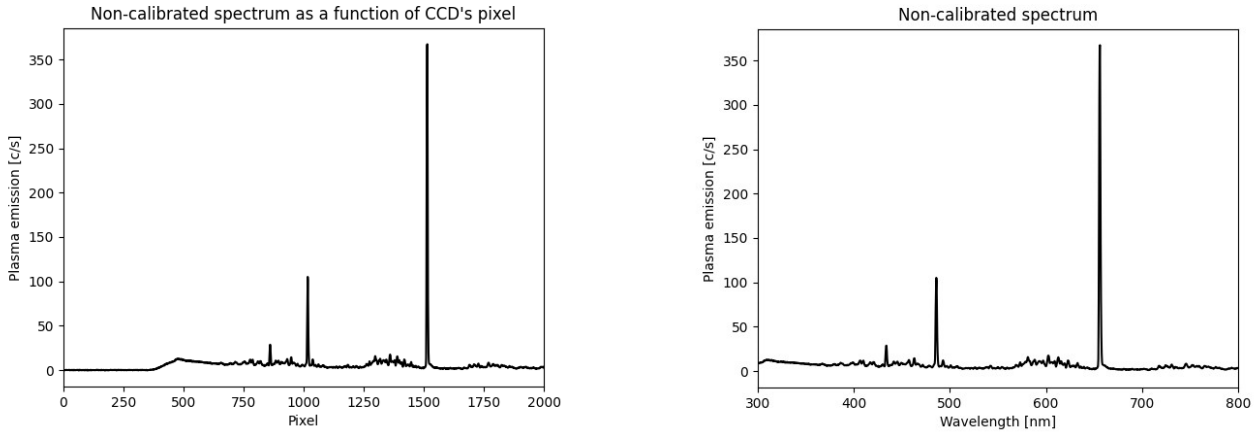

Figure 2.3: Intensities of shot number 5226 as a function of the CCD pixels (left) and of wavelengths (right)

2.1.2 Intensity calibration

The emissivity values of the Ulbricht sphere, contained in the instrument data sheet, are shown in Figure 2.4, as a function of the wavelength. First, the unit of measurement in $Wm^{-2}sr^{-1}$ of the spectral radiance of the Ulbricht sphere is converted to *photons* $m^{-2}s^{-1}$ by using equation 1.29. The conversion result is shown in figure 2.5 only for the range of wavelengths of interest.

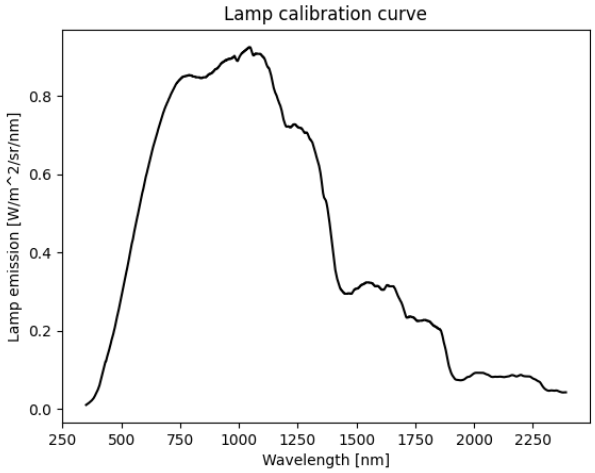

Figure 2.4: Lamp emission of the Ulbricht sphere in unit $Wm^{-2}sr^{-1}nm^{-1}$

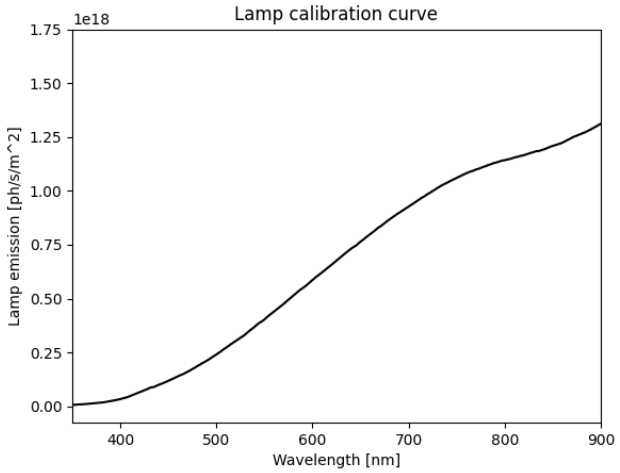

Figure 2.5: Lamp emission of the Ulbricht sphere in unit $photons\ m^{-2}s^{-1}$

As second step of the calibration procedure, Figure 2.6 shows the emission of the Ulbricht sphere measured with the spectrometer. The curve Iin blue shows the emission measured for setup 0, the one in red the emission for setup 1. The comparison between the two curves shows that the two $ND1$ filters reduced the emission intensity by a factor 26.

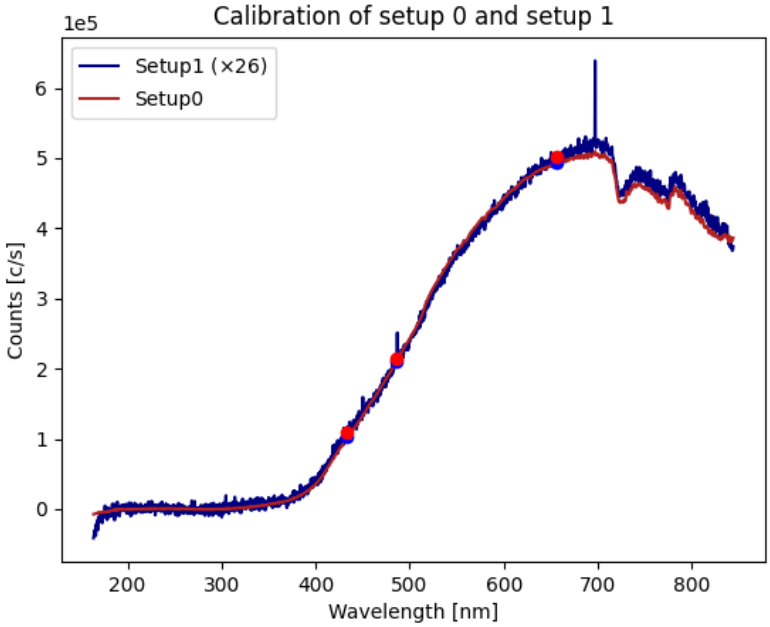

Figure 2.6: Calibration of setup 0 and setup 1. Setup 1 is multiplied by a factor 26 to show the compatibility in the shape of the two curve and the decrease in intensity after the two ND filters insertion.

Then, dividing the lamp emission curve (Figure 2.5) by the recorded spectrum for both the setups (Figure 2.6), the conversion factors are obtained. In Figure 2.7 the dependence of the calibration curve on the wavelenght is shown, while Table 2.2 includes the calibration factors for the first three Balmer lines, in the two different setups.

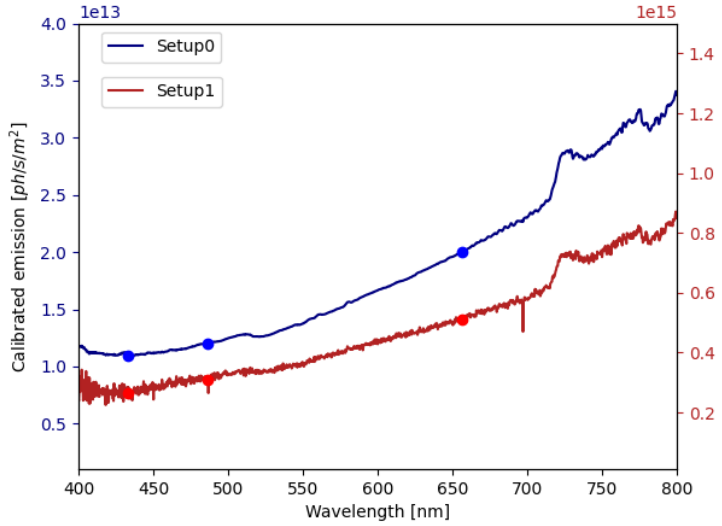

Figure 2.7: Calibration curve

Balmer line	Calibration Factor ($\times 10^{13}$ $[ph\, m^{-2} s^{-1}]$)	Setup
H_α	1.99	0
H_β	1.20	
H_γ	1.09	
H_α	51.1	1
H_β	30.8	
H_γ	26.4	

Table 2.2: Calibration factors for the Balmer lines in the two setups.

Figure 2.8 shows the recorded spectrum, already normalized to the exposure time. The recorded spectrum is obtained by measuring the plasma intensity with the same spectrometer used for the intensity calibration procedure, described in Section 2. By using the calibration curve of Figure 2.7 multiplied by the raw spectrum, the calibrated spectrum of Figure 2.9 is obtained.

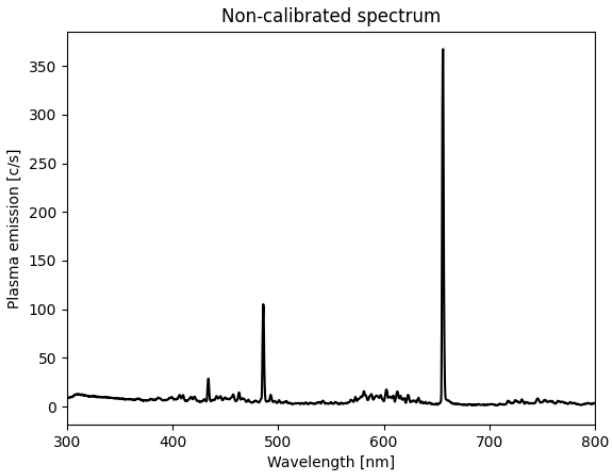

Figure 2.8: Non-calibrated spectrum

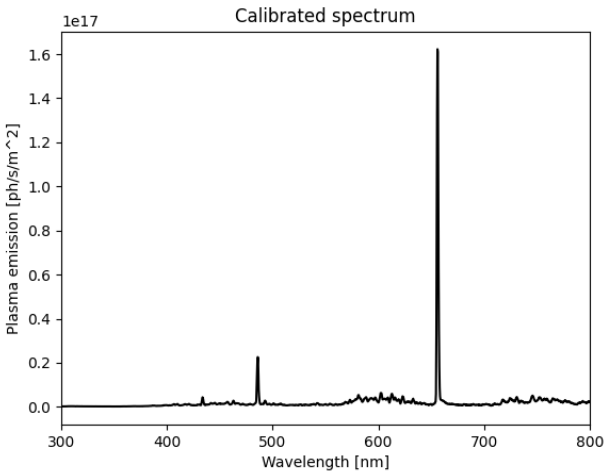

Figure 2.9: Calibrated spectrum

It is worth noticing that the raw and the calibrated spectra differ in the proportion between the intensities of the three Balmer lines.

2.2 Data analysis

2.2.1 Time trend analysis

This section focuses on the analysis of the time trace of H_α and H_β emission during the pulse evolution. Figure 2.10 shows the time trend of both emission intensities along with the control parameters.

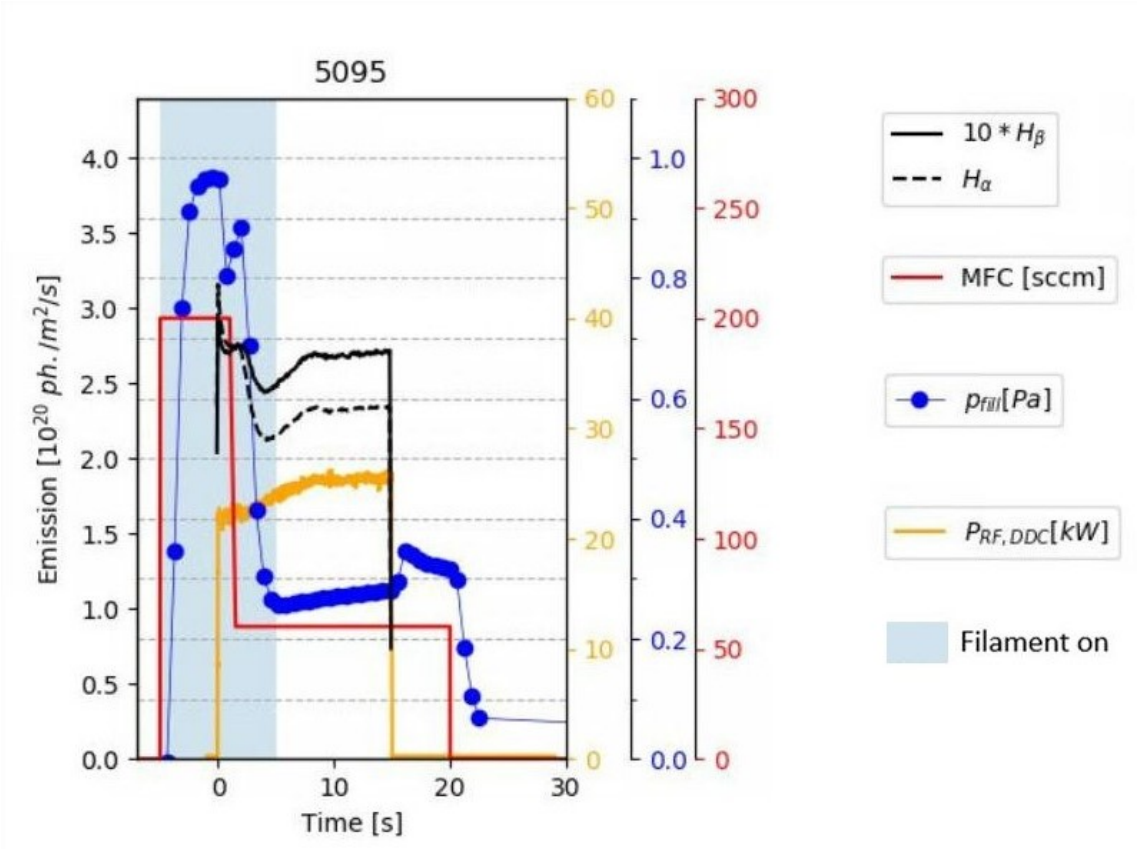

Figure 2.10: Time trend of shot 5095 for different signals: the blue background identifies the time zone in which the filament is on, in red the MFC settings, in blue the source pressure, in yellow the RF power measure with the dual directional coupler, the black continuous line is the H_α emission and the dotted black line is the H_β emission.

In every pulse, time zero corresponds to the moment at which the RF power is switched on. The gas injection into the expansion chamber is controlled by the mass flow controller (MFC). The pressure measurements follow the same trend as the MFC setting with a short delay (i.e. about $2\,s$). The filament is switched on simultaneously with the gas injection start, and is needed to provide the initial electrons to start the plasma ignition; it is turned off shortly after the RF power start.

It can be seen from the graph in figure 2.10 that the emission of H_α and H_β starts with the RF power, showing that the plasma is initiated very rapidly. It can also be noticed that the RF power does not reach the pre-set value immediately at the beginning, but follows a short ramp. Inductive coupling plasmas are characterized by an energy transfer between the variable magnetic field and the induced non-conservative electric field; in order for the RF power to transfer the maximum energy possible, the load impedance must match as much as possible the impedance of the power supply. The MINION experiment can be schematized as an RLC circuit with a variable load with the plasma being itself an impedance. If the RF power value is set to high values (e.g. $60\,kW$) and the plasma does not ignite, part of the power returns back to the driver elements, and it may result in harmful breakdown. Therefore, the internal capacitance of the RF generator is changed so as to adapt the precise frequency injected into the circuit, to the best coupling. At the beginning, in case the plasma fails to ignite, the RF power is kept low enough to avoid damages. Then the RF power is raised, and the intrinsic time response of the system requires several seconds to attain the set RF power value.

When the RF power starts, the pressure measurements in the source exhibits a sudden drop, followed by a raise after the RF power is switched off. This is due to H_2 depletion, i.e. H_2 is dissociated into H atoms, thus resulting in an apparent reduction of the H_2 pressure. When the MFC is set at the value corresponding to the desired pressure, the emissions are affected by a decrease in intensity, suggesting the correlation between particle density and line intensities. On the contrary, as the RF power is

increased up to the desired value, the intensities of H_α and H_β increase with the plasma density until they reach a plateau, where their values are stable.

At the end of the plasma pulse, the RF power is turned off, with the aforementioned increase in pressure, and finally the MFC is set to stop gas injection.

2.2.2 Parameter variation analysis

In this section, the intensity of the H_α and H_β emissions is studied, in order to have accurate values to use for further analysis of the plasma parameters.

The intensity of the H_α and H_β lines is derived from the Gaussian fit of the specific lines in different absolutely calibrated spectra collected in the following pulses: 5095, 5099, 5100, 5150, 5154. These spectra are measured with different pressure values and RF power values, in order to investigate the plasma behaviour.

The parameters are shown in Table 2.3.

shot number	$p_{fill}\,[Pa]$	pre-set $P_{RF}\,[kW]$		measured $P_{RF}\,[kW]$		$t_{start}\,[s]$		$t_{stop}\,[s]$	
5095	0.3	30		25.38 ± 0.01		8.3		14.7	
5099	0.3	50		41.38 ± 0.02		11.1		15.0	
5100	0.3	60		49.21 ± 0.02		11.5		15.0	
5150	0.6	40	60	32.87 ± 0.02	49 ± 1	10.6	12.4	8.0	9.5
5154	0.3	40	60	33.08 ± 0.02	49.33 ± 0.02	10.4	12.7	8.1	9.4

Table 2.3: Pressure in the source and RF power (pre-set and measured) values for each analysed shot. t_{start} and t_{stop} are the values of time within which the measured P_{RF} values have been estimated.

Both in pulse number 5150 and 5154 two stationary values of the RF power were specified, so both conditions can be studied, at the same pressure.

Figure 2.11 shows that the intensities of H_α, H_β and H_γ of calibrated spectra increase with the RF power. In particular, Figure 2.11 shows pulses number 5095, 5099, 5100 and 5154 (although this pulse has two values of RF power, only its lower RF power value is taken into account in the present analysis), to study the dependence of the intensity of the three Balmer lines on the RF power at a pressure of $0.3\,Pa$.

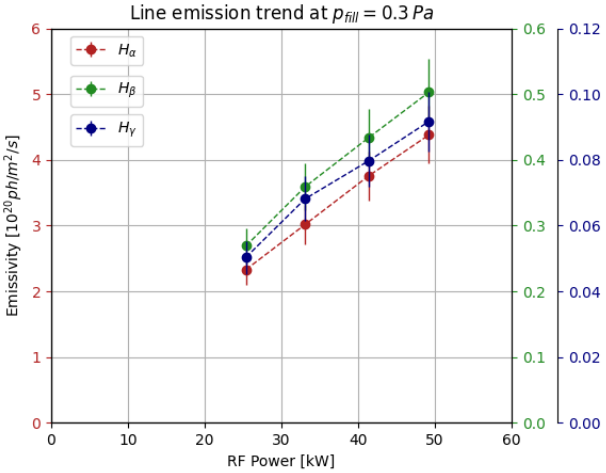

Figure 2.11: Dependence of the intensities on the RF power at a pressure of $0.3\,Pa$.

In particular, in this figure, each Balmer line is highlighted in a different color and refers to the axis with the same color. As visible in the graph, H_α lines are far more intense than H_β and H_γ, but all

three of them increase in intensity as the RF power increases. The errorbars are determined by taking into account many factors that affect the measure, such as the spread of the line of sight cone of view [17]; these errors collectively contribute to about 10% of each measure.

As described by Equation 1.11, the explanation for the increase of line emission with RF power lies in the dependence of the emitted light on the population density. As the RF power increases, the energy transferred from the RF circuit to the plasma increases, with the result that the particles in the chamber acquire more energy; consequently, more collisions take place. As a result of the two main reactions (1.19 and 1.22), more electrons and more hydrogen atoms are created. This increases the population density and consequently the line emission, as shown in the figure above.

As for the dependence of the emitted light on the source pressure, the following graph shows a comparison between H_α emission at $p_{fill} = 0.3\,Pa$ and at $p_{fill} = 0.6\,Pa$. The data at $0.3\,Pa$ are related to shot number 5095, 5099, 5154, while the ones at $0.6\,Pa$ to shot number 5150.

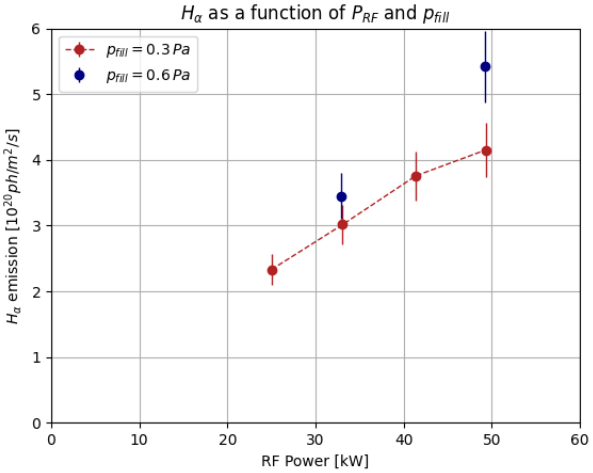

Figure 2.12: Comparison between two different values of pressure for H_α emissions.

Like in the previous graph, as the RF power increases, the intensities increase. It can also be noticed that pressure and H_α emission are directly correlated. Between $30\,kW$ and $40\,kW$, as the pressure doubles, the H_α intensity change by a factor lower than 1. Instead, when the RF power is higher (about $50\,kW$) the emission changes by a bigger factor. Either way, the RF power influences the line intensities more than the pressure. In fact, as can be seen in Figure 2.11, doubling the RF power[3] changes the intensity of H_α by a factor of about 2, suggesting a direct proportionality between the two physical quantities.

2.3 Determination of plasma parameters

The aim of this section is to determine the electron density in the driver region by means of the line ratio method, previously discussed in section 1.6.

The line ratio method takes as a prerequisite of the analysis the knowledge of the electron temperature in the region involved in the analysis -in this case, the driver-. The data regarding the electron temperature come from LP measurements. The probe is held, as mentioned above, by a manipulator that can position it at different depths inside the driver. Figure 2.13 shows the electron temperature measured at a fixed pressure value of $0.3\,Pa$ for two different values of RF power, $40\,kW$ and $60\,kW$. The horizontal axis in the following figure is the axial distance in the source: 0 is the PG position and $37\,cm$ is the driver backplate.

[3]Shot number 5095 has a measured RF power value of 25.4 and shot number 5100 has a value of 49.2, so it is safe to consider their ratio to be of about 2.

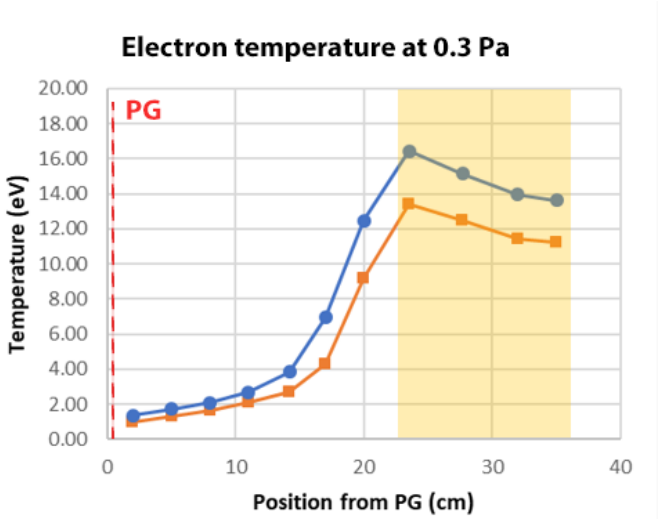

Figure 2.13: Electron temperature as a function of the Langmuir probe position, at $p_{fill} = 0.3\,Pa$ and for two different RF power values: in blue $P_{RF} = 60\,kW$, in orange $P_{RF} = 40\,kW$

Figure 2.14 shows the changes of the electron temperature inside the driver -at $27\,cm$ from the PG- as the pressure changes in a range from $0.3\,Pa$ and $0.6\,Pa$, for the same two values of RF power: $40\,kW$ and $60\,kW$. For the case at $0.3\,Pa$, the electron temperature values are highlighted in yellow. The pressure range that is target for the MINION experiment is highlighted in yellow.

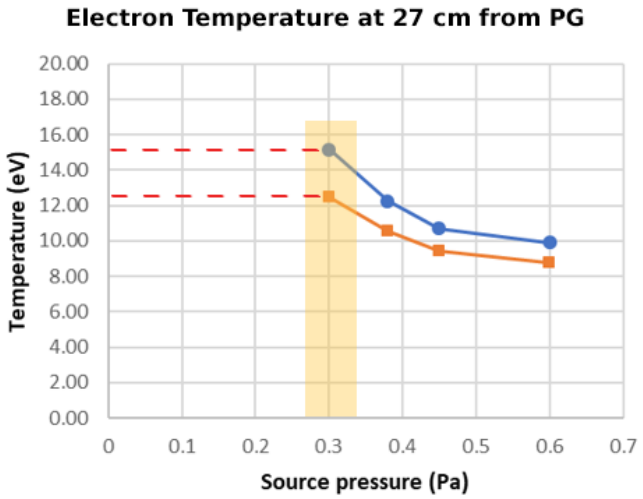

Figure 2.14: Electron temperature as a function of the source pressure, at $LPposition = 27\,cm$ and for two different RF power values: in blue $P_{RF} = 60\,kW$, in orange $P_{RF} = 40\,kW$

The graph presented above shows that the electron temperature range in the driver is, two different values of RF power, between $12\,eV$ and $15\,eV$ for measurements at $0.3\,Pa$ and between $9\,eV$ and $10\,eV$ for measurements at $0.6\,Pa$.

Therefore, the line that regards plasma parameters in the driver at $0.3\,Pa$ is the green one in figure 2.15, while the line for $0.6\,Pa$ is the pink one. The graph, realized with the data produced by the YACORA code[16][5], shows the effective emission rate coefficient ratio as a function of electron density, taking into account only the direct excitation channel (1.19); The effective rate coefficient ratio $X_{\alpha}^{eff}/X_{\beta}^{eff}$ is shown.

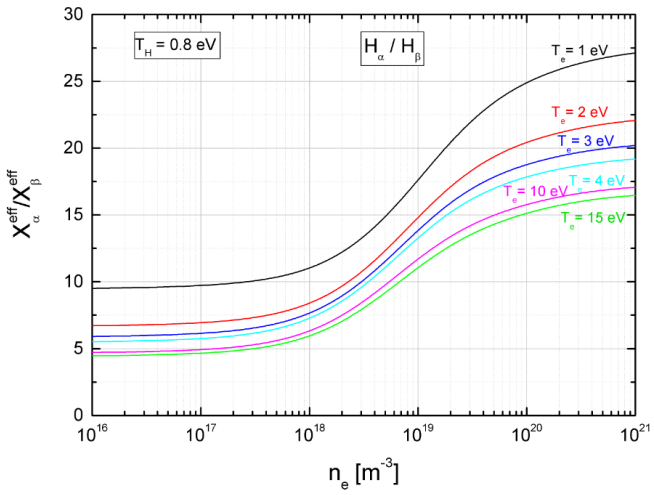

Figure 2.15: Dependence of the ratio between effective emission rate coefficient on the electron density. The specified T_H refers to the temperature of hydrogen atoms, which is negligible with respect to the electron temperature.

The experimental line ratio H_α/H_β from the calibrated spectra is reported in Figure 2.16. The errorbars have been estimated as explained in section 2.2.

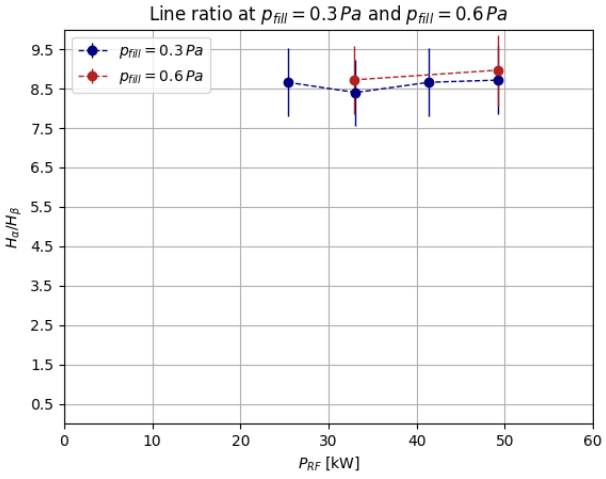

Figure 2.16: Line ratio at $p_{fill} = 0.3\,Pa$ and $p_{fill} = 0.6\,Pa$

The mean value of the line ratios at $0.3\,Pa$ and at $0.6\,Pa$ are reported in Table 2.4 along with the electron densities deduced from Figure 2.15 by intersecting the $T_e = 15\,eV$ curve with the mean value of the line ratios at $0.3\,Pa$ and the $T_e = 10\,eV$ curve with the mean value of the line ratios at $0.6\,Pa$, as shown in Figure 2.17 and Figure 2.18. The chosen temperature curves are the ones closer to the electron temperature values measured with the LP probe at the two values of pressure.

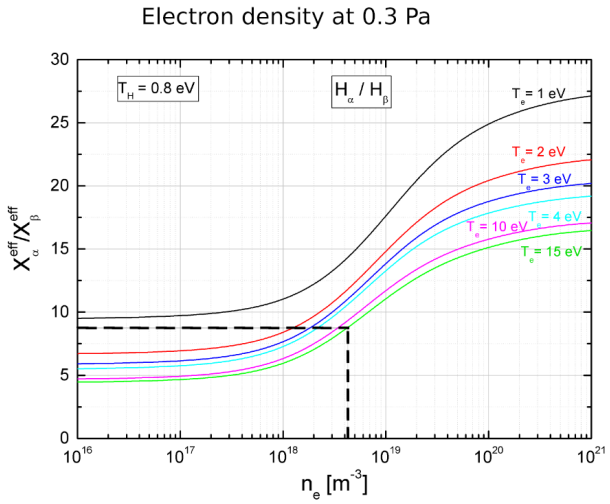

Figure 2.17: Electron density at $0.3\,Pa$

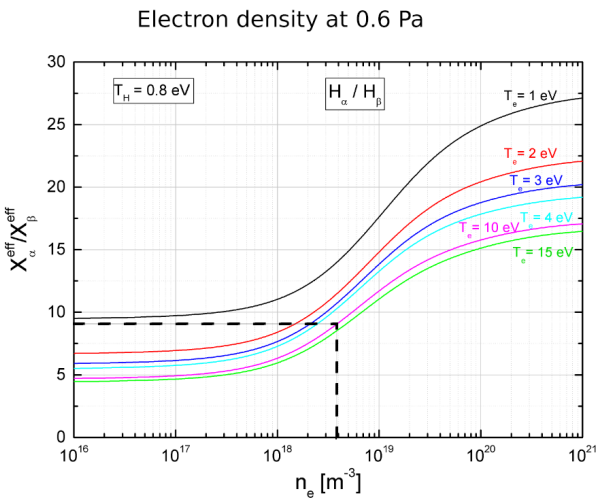

Figure 2.18: Electron density at $0.6\,Pa$

parameter	value	
$p_{fill}\,[Pa]$	0.3	0.6
mean line ratio value	8.6	8.8
$n_e\,[m^{-3}]$	$4 \cdot 10^{18}$	$4 \cdot 10^{18}$

Table 2.4: The error bar on the electron density has to be considered of about 30%, estimated by considering the error on line ratio value.

This results are to be confronted with the values of the LP. The values of electron density from the Langmuir probe are reported in Table 2.5. The density values are obtained by applying a model to the current that the probe measures; among the different theories for LP analysis, the one used in MINION is the one that better satisfies the plasma conditions of the experiment [15].

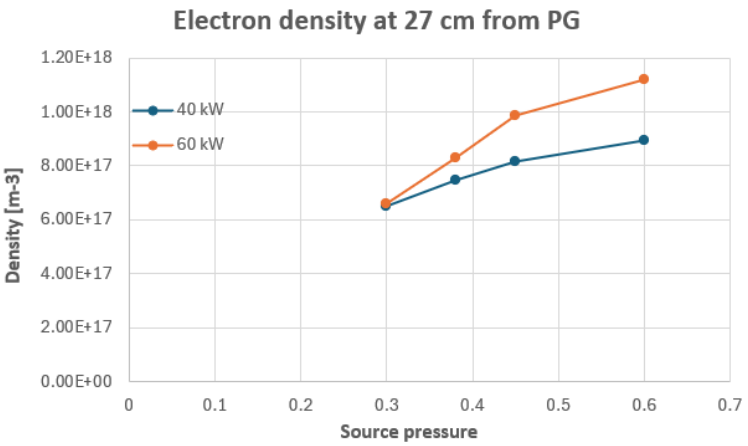

n_e x$10^{17}[m^{-3}]$	$p_{fill}\,[Pa]$	$P_{RF}\,[kW]$
6.5	0.3	40
9.0	0.6	
6.6	0.3	60
11.2	0.6	

Table 2.5: Values of electron density at different value of source pressure and RF power, measured with LP.

Figure 2.19: Density values in the driver, measured with Langmuir probe.

The values obtained are one order of magnitude lower than the one deriving from the OES measurement and listed in Table 2.4. While still being greatly different, the electron density values between the LP and the OES measurements at $0.6\,Pa$ are closer to each other than the ones at $0.3\,Pa$. The value at $0.6\,Pa$ and $60\,kW$ has the same order as magnitude of the values derived by OES measurements.

It is to be noted that this is the first time that a direct comparison between plasma parameters from two different diagnostic systems is carried out in MINION. The electron density values obtained for

the two pressures are not compatible with the values deduced from the CR model; however, agreement within less than a factor of 10 is already satisfying.

In the following, some considerations are given regarding the discrepancy between the electron density estimates obtained from the two diagnostic systems.
Concerning the principle of operation of the Langmuir probes, the electron density that the probe measures is the current in the close vicinity of the probe itself, inside the border of the Debye sheath (see Section 1.4); those values have to be converted into more representative values. This conversion is done by taking into account the relative density of the different species that populate the plasma, the Debye length, the sheath and the collection of charges at the probe electrode. Despite the simplicity of the measurements, there are different models describing the collection of the charged species. Furthermore, as the plasma is created, the concentrations of ions and electrons change, making it difficult to identify a constant conversion factor to apply to the measurements during the plasma pulse.

At the same time, the emission measurement is integrated along a line-of-sight, which means that the data collected take into account the average values along the LOS.

Concerning the collisional radiative model used for the plasma parameter estimation, it accounts for only one excitation channel, namely excitation by electron impact (1.19). Other processes should be included in the model, such as dissociative recombination (1.23) and dissociation of H_2 (1.22). By including additional excitation channels, the estimated electron density decreases.

Another point to consider is the effect of the particle density profile along the line of sight, which has not been considered in the present work. At low electron temperature, recombining processes occurring in the expansion region can contribute to the emission measured by the OES system and might not be negligible.

Last but relevant for the case under discussion, there might be an effect due to the non-Maxwellian distribution of the electron population: the lower the pressure, the less accurately the Maxwellian distribution describes the electron energy distribution. Thus, the outcome of CR models might not be fully representative of the plasma emission. Consequently, it is reasonable that the data measured at $0.6\,Pa$ better match the OES results.

Chapter 3

Conclusions and perspectives

The ITER experiment requires high temperatures in the plasma region to reach thermonuclear fusion. To this purpose, part of the heating power, $330MW$, will be provided by Neutral Beam Injectors (NBI), based on the generation, acceleration and neutralization of negative ions. At the ITER Neutral Beam Test Facility in Padova, the MINION experiment was realized to optimize the NBI source particularly by investigating whether the plasma parameters and beam performances would benefit from specific modifications of the ion source design. This thesis focused on estimating the plasma electron density in the very first campaign of the MINION experiment by means of spectroscopic investigations.

Whereas the electron temperature was estimated using the Langmuir probes, the electron density was studied with optical emission spectroscopy. The temperature estimation was crucial because its value was needed to estimate with a collisional radiative model the excited state density of the H atom and to predict the atomic emission in the plasma.To estimate the electron density, the line ratio method is applied, which consists in comparing the ratio between the Balmer lines H_α and H_β with the predicted value from collisional radiative model.

At first, the experimental setup was calibrated using a mercury lamp for the conversion between the CCD pixels and wavelength value and an integrating sphere to convert the number of counts per second measured with the spectrometer in number of photons per unit time per unit area.

Satisfying first measurements were performed in MINION under different conditions of RF power and pressure and the analysis of the calibrated spectrum data led to an experimental estimate of electron density in the order of 10^{18}. By comparing those results with the ones obtained using the Langmuir probes, differences were found and are discussed in the thesis. The explanation for the difference between the two measurements is related to the fact that only the excitation channel from electron impact is included at this stage in the CR model, that the OES measurement is line-of-sight integrated so that it does not account for spatial inhomogeneities of the plasma parameters, and that non-Maxwellian distribution of the electrons may be present, especially at lower pressure values, i.e. $0.3\,Pa$.

Further developments of this work may regard the study of different parts of the plasma, by extending the measurements to the boundary region of the driver, and to the expansion region by using additional line of sights. The experiment is already provided with another LOS (*LOS 2* in Figure 2.1), that will be used to obtain data regarding the boundary region of the driver. Installing another LOS will allow to study the plasma in the vicinity of the plasma grid. On the other hand, focusing on the study carried out in this work, a way of improving the data analysis may include implementing the calculation by including the Fulcher band, to have more effective emission coefficients ratio and therefore to have more estimations of the electron density of the same point in the plasma. Also, the CR model may be enhanced by considering not only direct excitation but also dissociative excitation channels (Equation 1.22) and dissociative recombinations (Equation 1.23).

In parallel, the source will be upgraded along with the diagnostic capabilities.

Bibliography

[1] M Bigi et al. "A model for electrical fast transient analyses of the ITER NBI power supplies and the MAMuG accelerator". In: *Fusion engineering and design* 84.2-6 (2009), pp. 446–450.

[2] KF Carr. "Integrating sphere theory and applications Part II: integrating sphere applications". In: *Surface coatings international* 80.10 (1997), pp. 485–490.

[3] Ursel Fantz. "Basics of plasma spectroscopy". In: *Plasma sources science and technology* 15.4 (2006), S137.

[4] Takashi Fujimoto and RWP McWhirter. "Validity criteria for local thermodynamic equilibrium in plasma spectroscopy". In: *Physical Review A* 42.11 (1990), p. 6588.

[5] Maurizio Giacomin. *Application of collisional radiative models for atomic and molecular hydrogen to a negative ion source for fusion*. 2017.

[6] RS Hemsworth et al. "Overview of the design of the ITER heating neutral beam injectors". In: *New Journal of Physics* 19.2 (2017), p. 025005.

[7] EDA ITER. "Agreement and Protocol 2". In: *ITER EDA Documentation Series* 1 (1994).

[8] *ITER EDA Agreement and Protocol 2*. ITER EDA Documentation Series 5. Vienna: INTERNATIONAL ATOMIC ENERGY AGENCY. URL: https://www.iaea.org/publications/5252/iter-eda-agreement-and-protocol-2.

[9] Isabella Mario. "Correlation between plasma and beam properties at the ELISE test facility". PhD thesis. Augsburg Universitaet, 2020.

[10] P-H Rebut et al. "ITER: the first experimental fusion reactor". In: *Fusion engineering and design* 30.1-2 (1995), pp. 85–118.

[11] Y Shimomura et al. "ITER towards the construction". In: *Fusion engineering and design* 74.1-4 (2005), pp. 9–16.

[12] Y Shimomura. "Overview of International Thermonuclear Experimental Reactor (ITER) engineering design activities". In: *Physics of plasmas* 1.5 (1994), pp. 1612–1618.

[13] P al Sonato et al. "The ITER full size plasma source device design". In: *Fusion Engineering and Design* 84.2-6 (2009), pp. 269–274.

[14] National Institute of Standards and Technology. *Security Requirements for Cryptographic Modules*. Tech. rep. Federal Information Processing Standards Publications (FIPS PUBS) 140-2, Change Notice 2 December 03, 2002. Washington, D.C.: U.S. Department of Commerce, 2001. DOI: 10.6028/nist.fips.140-2.

[15] Peter C Stangeby et al. *The plasma boundary of magnetic fusion devices*. Vol. 224. Institute of Physics Pub. Philadelphia, Pennsylvania, 2000.

[16] D Wünderlich et al. "Yacora on the Web: Online collisional radiative models for plasmas containing H, H2 or He". In: *Journal of Quantitative Spectroscopy and Radiative Transfer* 240 (2020), p. 106695.

[17] B Zaniol, R Pasqualotto, and M Barbisan. "Design of a beam emission spectroscopy diagnostic for negative ions radio frequency source SPIDER". In: *Review of Scientific Instruments* 83.4 (2012).